



## Research paper

## Reynolds number and settling velocity influence for finite-release particle-laden gravity currents in a basin

E.P. Francisco <sup>a</sup>, L.F.R. Espanhol <sup>a</sup>, S. Laizet <sup>b,\*</sup>, J.H. Silvestrini <sup>a</sup><sup>a</sup> Faculdade de Engenharia, Pontifícia Universidade Católica do Rio Grande do Sul, Av. Ipiranga 6681, 90619-900, Porto Alegre, RS, Brazil<sup>b</sup> Turbulence, Mixing and Flow Control Group, Department of Aeronautics Imperial College London, London, SW7 2BY, United Kingdom

## ARTICLE INFO

## Keywords:

Particle-laden gravity current  
Energy budget  
Deposition of particles  
Direct numerical simulation

## ABSTRACT

Three-dimensional highly resolved Direct Numerical Simulations (DNS) of particle-laden gravity currents are presented for the lock-exchange problem in an original basin configuration, similar to delta formation in lakes. For this numerical study, we focus on gravity currents over a flat bed for which density differences are small enough for the Boussinesq approximation to be valid. The concentration of particles is described in an Eulerian fashion by using a transport equation combined with the incompressible Navier-Stokes equations, with the possibility of particles deposition but no erosion nor re-suspension. The focus of this study is on the influence of the Reynolds number and settling velocity on the development of the current which can freely evolve in the streamwise and spanwise direction. It is shown that the settling velocity has a strong influence on the spatial extent of the current, the sedimentation rate, the suspended mass and the shape of the lobe-and-cleft structures while the Reynolds number is mainly affecting the size and number of vortical structures at the front of the current, and the energy budget.

## 1. Introduction

Turbidity currents are particle-laden gravity-driven currents in which the gravitational driving force is supplied by a density excess associated with the suspension of particles. They exhibit a complex dynamic with the presence of the lobe-and-cleft patterns at the head of the current followed by a region of mixing with intense spanwise Kelvin-Helmholtz vortices. Understanding the physical mechanism associated with these currents as well as the correct prediction of their main features are of great importance for practical and theoretical purposes. This type of gravity-driven currents is the most important mechanism for the dispersal and deposition of sand on deep seafloors and on underwater slopes of many deltas and lakes. Their associated deposits can provide a valuable record of submarine landslide dynamics, shedding light on the magnitude of associated tsunamis, river flooding and major earthquakes (Talling et al. (2012)). They can also damage seriously seafloor cables and expensive seafloor installations for recovering oil and gas (Barley (1999)). More details about turbidity currents can be found in the extensive reviews of Meiburg and Kneller (2009) and Middleton (1993).

The deposits observed in nature are very complex, very voluminous and are extremely challenging and costly to study. As a result, turbidity currents have been mainly investigated in very simplified and idealized

configurations. The most studied one is the horizontal channelized lock-exchange configuration in which uniformly suspended particle sediments are enclosed in a small reservoir separated by a gate from the fresh fluid. The dynamics of channelized currents is reasonably well understood with a large number of experimental, numerical and theoretical studies as well as predictive models (Middleton (1993); Meiburg and Kneller (2009)).

The first experimental investigations on non-channelized turbidity currents were reported in the 1950's by Kuenen (1951) with experimental studies of deposition patterns for turbidity currents in a basin configuration. Large-scale laboratory experiments, similar to the present configuration, are presented in Luthi (1981) to investigate the dilution process of the particles with the ambient fluid with a focus on the thickness of the deposit. In Bonnecaze et al. (1995), the authors studied experimentally axisymmetric gravity currents with a finite-release of particles to determine both the radius of an axisymmetric particle-laden gravity current as a function of time and its deposition pattern for a variety of initial particle concentrations, particle sizes, volumes and flow rates. More recently, Parsons et al. (2007) showed evidence of a mechanism called lobe switching (focusing of the flow into a single lobe) in their laboratory experiments for a basin configuration.

Highly resolved simulations of conservative gravity currents (with no suspended sediment) for non-channelized axisymmetric initial reservoirs

\* Corresponding author.

E-mail address: [s.laizet@imperial.ac.uk](mailto:s.laizet@imperial.ac.uk) (S. Laizet).

were performed in [Cantero et al. \(2007b,a\)](#) for various Reynolds numbers. The objective was to address the structure and dynamics of cylindrical density currents and in particular to clarify the influence of circumferential stretching. The authors made some comparisons with a laboratory experiment for the case of saline water spreading in quiescent fresh water but with a much higher Schmidt number by comparison to the simulations. They found that their numerical simulations were in good agreement with experimental observations and with theoretical prediction models for axisymmetric currents ([Hoult \(1972\)](#); [Huppert and Simpson \(1980\)](#); [Rottman and Simpson \(1983\)](#); [Ungarish \(2009\)](#)).

Very recent high-fidelity simulations and laboratory experiments for circular and non-axisymmetric finite initial reservoirs ([Zgheib et al. \(2015a,c\)](#)) showed that the effect of an initial non-circular shape for the lock can persist for the whole duration of the observation, making most of prediction models irrelevant. The authors found that some of their non-axisymmetric currents eventually reach a self-similar shape with the same power-law spreading rate as an axisymmetric front. They also identified that the local speed of propagation is strongly dependent of the initial reservoir's shape, leading to local fast and slow fronts. They proposed an advanced box model, extending the classical box model ([Huppert and Simpson \(1980\)](#)), in order to account for the shape of the initial release ([Zgheib et al. \(2014, 2015b\)](#)). Theoretical and experimental tentatives to predict gravity currents in open basins was also made by [Rocca et al. \(2008, 2012\)](#). The authors used a complex model based on shallow-water theory for the prediction of the evolution of gravity currents. They found that currents in an open basin cannot be predicted using the usual framework adopted for channelized and axisymmetric gravity currents.

The main motivation behind the present numerical work is to study idealized gravity currents in an original basin configuration more representative of real situations than channelized and axisymmetric gravity currents. As a first step, we focus exclusively on the influence of the Reynolds number and settling velocity in the early stages of the evolution of the current. The paper is organized as follows. We first present the Direct Numerical Simulation (DNS) methodology, the flow configuration and the numerical parameters of each simulation. Some instantaneous visualizations followed by results about the spreading of the current, sedimentation rate, suspended mass and energy budget are discussed in the following sections. Then, the structure of the current at the wall and related deposition are discussed in great details. The paper is ended with a conclusion.

## 2. Numerical set-up

The flow configuration is shown in [Fig. 1](#). Unlike axisymmetric lock-exchange configurations or the non-axisymmetric configuration of [Zgheib et al. \(2014, 2015b\)](#), there is a preferential direction for the current, perpendicular to the initial reservoir ( $x_1$ -axis, streamwise direction). We assume a small volume fraction of the particles (typically less than 1%) so that interactions among the particles can be neglected as

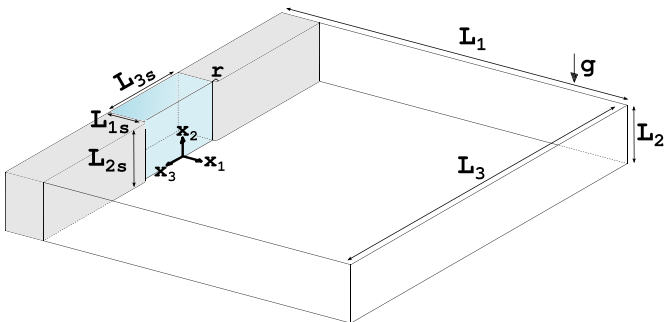


**Fig. 1.** Schematic view of the initial configuration of the lock-exchange open basin problem.

discussed in [Espath et al. \(2015\)](#). In this framework, the settling velocity  $u_s$  may be considered constant and is related to the particle diameter by the Stokes settling velocity law ([Julien \(2010\)](#)) which assumes that the dominant flow force on an individual particle is the Stokes drag. This flow configuration can be studied by solving the incompressible Navier-Stokes equations and a scalar transport equation under the Boussinesq approximation for the concentration of particles.

To make the equations dimensionless, half of the box height  $h$  and the buoyancy velocity  $u_b$  are chosen as the characteristics length and velocity scales, respectively. The buoyancy velocity is related to the reduced gravitational acceleration  $u_b = \sqrt{g'h}$  where  $g' = g(\rho_p - \rho_0)c_i/\rho_0$ . Here, the particle and ambient fluid densities are  $\rho_p$  and  $\rho_0$  respectively, with  $g$  defined as the gravitational acceleration, and  $c_i$  as the initial volume fraction of the particles in the lock. The Reynolds number is defined as  $Re = u_b h / \nu$  where  $\nu$  is the kinematic viscosity, and the Schmidt number is defined as  $Sc = \nu/\kappa = 1$ , where  $\kappa$  is the mass diffusivity of the particle-fluid mixture. All other variables are made dimensionless using  $c_i$ ,  $h$  or/and  $u_b$ . Thus, the incompressible Navier-Stokes equations and scalar transport equation can be written as

$$\frac{\partial \mathbf{u}}{\partial t} = -\nabla p - \frac{1}{2}[\nabla \cdot (\mathbf{u} \otimes \mathbf{u}) + (\mathbf{u} \cdot \nabla) \mathbf{u}] + \nu \nabla^2 \mathbf{u} + ce^g + \mathbf{f} \quad (1)$$

$$\nabla \cdot \mathbf{u} = 0 \quad (2)$$

$$\frac{\partial c}{\partial t} + (\mathbf{u} + u_s \mathbf{e}^g) \cdot \nabla c = \kappa \nabla^2 c \quad (3)$$

where  $\mathbf{u}(\mathbf{x}, t)$  is the velocity,  $p(\mathbf{x}, t)$  the pressure,  $c(\mathbf{x}, t)$  the particle concentration,  $\mathbf{e}^g = (0, -1, 0)$  the unit vector in gravity direction and  $\mathbf{f}$  is a forcing term to account for the basin geometry.

These equations are solved on a Cartesian mesh with the high-order flow solver **Incompact3d**<sup>1</sup> which is based on sixth-order compact schemes for spatial discretization and a third-order Adams-Bashforth scheme for time advancement. To treat the incompressibility condition, a fractional step method requires to solve a Poisson equation, fully solved in spectral space. With the help of the concept of modified wavenumber, the divergence free condition is ensured up to machine accuracy. The pressure mesh is staggered from the velocity mesh by half a mesh to avoid spurious pressure oscillations. The modelling of the channel-basin geometry is performed with a customized immersed boundary method based on a direct forcing approach that ensures a zero-velocity boundary condition at the wall of the solid geometry and a no-flux boundary condition for the particle concentration. Following the strategy of [Paranaudeau et al. \(2008\)](#), a mirror flow is imposed inside the geometry in order to avoid any discontinuities at the wall of the geometry. Note that the edges of the basin have been rounded ( $r = 0.2$ , as seen in [Fig. 1](#)). For the particles concentration, no-flux conditions are imposed at the wall of the geometry and are consistent with the boundary conditions of the computational domain. More details about the present code can be found in [Laizet and Lamballais \(2009\)](#). The size of the present simulations is such that we have no alternative but to use the parallel version of this solver ([Laizet and Li \(2011\)](#)), based on a highly scalable 2D decomposition library and a distributed FFT interface. **Incompact3d** has been extensively validated for axisymmetric gravity currents (non-published comparisons with the data from [Zgheib et al. \(2015c\)](#)) and for channelized gravity currents ([Espath et al. \(2014, 2015\)](#); [de Rooij and Daziel \(2001\)](#)).

For the initial condition, a weak perturbation is introduced into the velocity field at the gate to mimic disturbances when the gate is removed. Free-slip boundary conditions are imposed for the velocity field in the streamwise and spanwise directions  $x_1$  and  $x_3$  while zero-velocity boundary conditions are used in the vertical direction  $x_2$  (to mimic

<sup>1</sup> This open source code is available at [www.incompact3d.com](http://www.incompact3d.com).

**Table 1**  
Summary of the numerical parameters.

	$Re$	$L_1 \times L_2 \times L_3$	$n_1 \times n_2 \times n_3$	$\Delta t$	$u_s$
REY1K2	1000	$12 \times 2 \times 12$	$1,201 \times 193 \times 1,201$	$4 \times 10^{-4}$	0.02
REY5K0	5000	$12 \times 2 \times 12$	$1,201 \times 289 \times 1,201$	$5 \times 10^{-4}$	0
REY5K2	5000	$12 \times 2 \times 12$	$1,201 \times 289 \times 1,201$	$5 \times 10^{-4}$	0.02
REY5K4	5000	$12 \times 2 \times 12$	$1,201 \times 289 \times 1,201$	$5 \times 10^{-4}$	0.04
REY5K8	5000	$12 \times 2 \times 12$	$1,201 \times 289 \times 1,201$	$5 \times 10^{-4}$	0.08
REY10K2	10,000	$12 \times 2 \times 12$	$1,201 \times 385 \times 1,201$	$4 \times 10^{-4}$	0.02

walls). For the scalar field, no-flux conditions are used in the streamwise and spanwise directions  $x_1$  and  $x_3$ , and in the vertical direction  $x_2$  at the top of the domain. For the particles sedimentation in the vertical direction  $x_2$  at the bottom of the domain, a simple 1D outflow boundary condition is imposed, meaning that the particles can virtually leave the computational domain to mimic the deposition process (non conservative simulations).

Six high-fidelity 3D simulations are presented in this paper and the parameters of the simulations are presented in Table 1. The initial volume of heavy fluid is defined as  $(L_{1s} \times L_{2s} \times L_{3s}) = (1 \times 2 \times 2)$ . The spatial and temporal resolutions have been determined consistently with previous high-fidelity 3D simulations of channelized and axisymmetric gravity currents (Espath et al. (2014, 2015); Zgheib et al. (2015c)) and the present results are independent of the spatial and temporal discretization. Three different Reynolds numbers and four different settling velocities are investigated with a focus on the early stages of the evolution of the current. At the end of our simulations more than 75% of the particles have deposited. In particular, for the simulation with the highest settling velocity more than 98% of the particles have left the computational domain, very close to the well-known run-out distance described in Ungarish (2009) for which all the particles have left the current. Note

finally that, in an equivalent laboratory experiment, the deposition of particles would imply a change in the topography of the bottom floor which could influence the evolution of the current and particle dynamics. In line with previous numerical studies based on high-fidelity simulations (Härtel et al. (2000b,a); Necker et al. (2002); Cantero et al. (2008); Espath et al. (2014)), this change of topography is not taken into account in the present simulations.

### 3. General features of the flow

Illustrations of our gravity currents in an open basin set-up for  $t = 10$  are presented in Fig. 2 using isocontours of the Q-criterion and the concentration of particles. For the simulations where the settling velocity is not zero, the current can be separated in three parts: (i) the head of the current where the well-known lobe-and-cleft patterns can be observed in combination with very intense vortical structures (if the Reynolds is high enough), (ii) a very quiet area just after the head with very low level of turbulence (even at high Reynolds number), (iii) a pocket of intense vortical activity, just in front of the gate, except for the simulation REY1K2 where the Reynolds number is too small to generate intense vortical structures. This alternation of intense and quiet areas was also observed for axisymmetric currents (Cantero et al. (2006, 2007b,a)). It can be noticed that regions of high concentration of particles coincide with regions of intense vortical activity (except for simulation REY1K2 with a low Reynolds number). As expected the area covered by the current at this time is strongly related to the settling velocity. Based on Fig. 2, the settling velocity (which is related to the particles size) does not seem to strongly affect the turbulence activity in the head of the current. This observational result will be checked afterwards when investigating the energy budget.

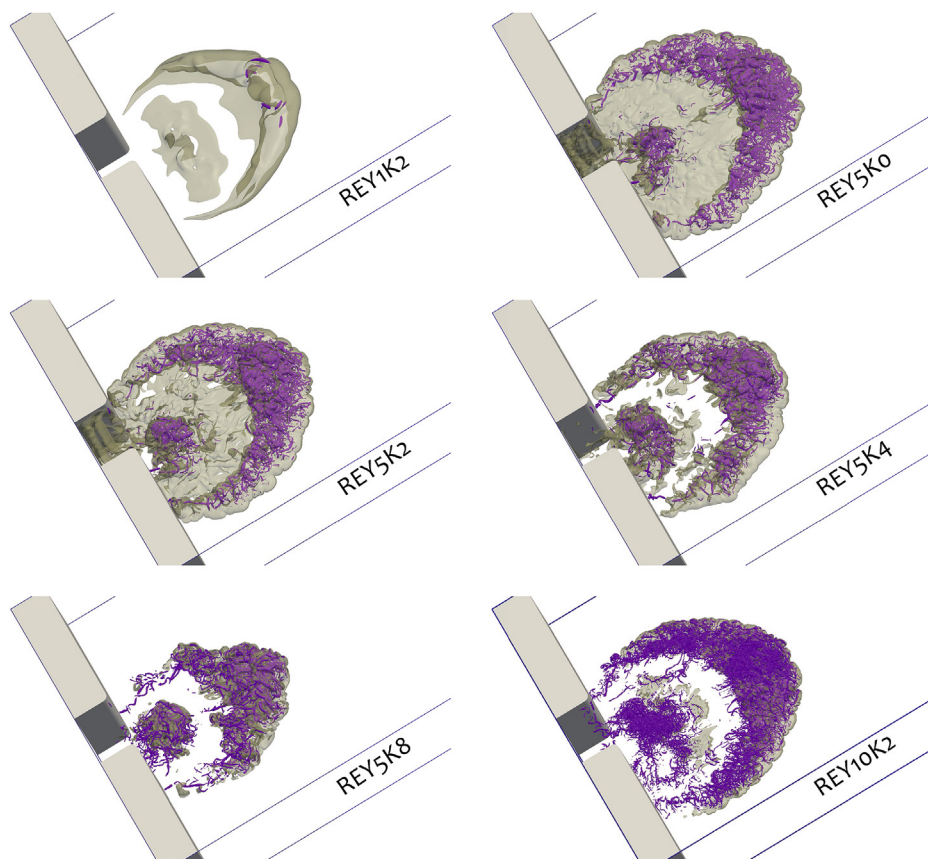


**Fig. 2.** Turbulent structures of the gravity currents illustrated by the Q-criterion for the isovalue  $Q = 25$  and by the concentration of particle  $c = 0.025$ . Data obtained at  $t = 10$ .

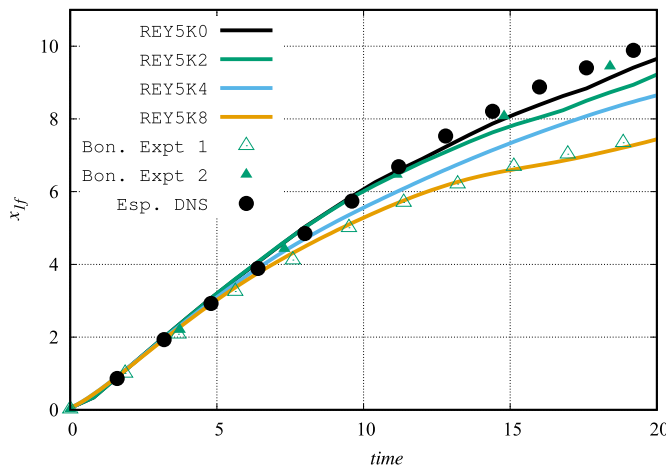


**Fig. 3.** Time evolution of the streamwise front location. The triangle symbols are extracted from the experiments of Bonnecaze et al. (1995) and correspond to a non-conservative (Expt 1) and a conservative axisymmetric (Expt 2) current. The black dot symbols are extracted from a channelized simulation of Espath et al. (2015), the lines are from the present study.

#### 4. Front location

The streamwise evolution of the front location is a quantity of importance, easily obtainable in experiments and simulations, which can be used to compare the difference between channelized, axisymmetric and the present basin gravity currents. Different phases of spreading have been identified when the current propagates horizontally into its ambient (Huppert and Simpson (1980); Cantero et al. (2007b)): (i) an acceleration phase where the current initially at rest reaches its maximum velocity, (ii) a slumping phase with a nearly constant front velocity, (iii) an inertial phase for which the buoyancy driving force is balanced by inertia and during which the current starts to decelerate, (iv) a viscous phase for which the buoyancy driving force is balanced by viscosity. For the non-channelized non-axisymmetric currents considered in this numerical study, the local front locations are expected to vary significantly with a strong dependence to the local direction of spreading. We therefore focus on the slowest and fastest directions of spreading, along the  $x_3$ -axis (spanwise front) and  $x_1$ -axis (streamwise front) respectively.

Comparisons with channelized and axisymmetric configurations for the streamwise evolution of the streamwise front location are presented in Fig. 3. The streamwise front location  $x_{1f}$  corresponds to the first streamwise location (located at  $x_3 = 0$ , corresponding to the middle-plane) for which the concentration is equal to 0.01 when starting from the end of the computational domain. A similar procedure is used for the spanwise location  $x_{3f}$ . The present results are consistent with the experimental data of Bonnecaze et al. (1995) for the simulations at Reynolds

5000 with and without suspended sediment. The experiments were carried out for axisymmetric initial reservoirs of conservative and non-conservative currents at comparable Reynolds numbers. The present data are also showing a slightly slower expansion for the present currents by comparison to a channelized gravity current. In the channel configuration, it is natural to expect a faster spreading of the current in the streamwise direction due to the presence of walls in the lateral direction which prevent the current to spread sideways.

The time evolution of the streamwise front location and of the ratio between the location of the streamwise and spanwise fronts are presented in Fig. 4. The power-law coefficients have been obtained with a conventional nonlinear least-squares (NLLS) Marquardt-Levenberg algorithm. For the present simulations, the slumping phase, with a linear time evolution, can be clearly observed up to  $t \approx 7.5$ , independently of the Reynolds number. After the slumping phase, the currents are transitioning very quickly to a phase where the front evolution scales as  $t^{1/3} - t^{2/3}$ , with a strong dependence to the settling velocity. Note that power-law exponents equal to 2/3 and 1/2 are usually reported for channelized currents and axisymmetric currents, respectively, in the inertial phase (Hoult (1972); Huppert and Simpson (1980); Rottman and Simpson (1983); Ungarish (2009)). The impact of the Reynolds number can be noticed with a slight reduction of the duration of the slumping phase for the simulation at the lowest Reynolds number. Other than that, it seems that the Reynolds number does not affect the power-law coefficient in the inertial phase.

The spanwise expansion of the current in the slumping phase is quite slow. It is however important to point out that for all the simulations the current is evolving a bit faster in the streamwise direction with reported power law coefficients of 1/5 – 2/5 for the ratio between the location of the streamwise and the spanwise fronts. Note that a power law coefficient of 1 corresponds to an axisymmetric spreading. For the simulation REY10K2, the evolution of the spanwise front is somehow irregular with an alternation of low and fast regions for the spanwise expansion. Due to the high settling velocity, the spreading of the current for the simulation REY5k8 is quite limited after  $t = 5$ , especially in the spanwise direction. Those results will be confirmed in Fig. 8 with isolines of the bottom wall concentration.

#### 5. Sedimentation rate, suspended mass and energy budget

In this section, the temporal evolution for the sedimentation rate and suspended particles mass is presented in Fig. 5. The sedimentation rate  $m_s(t)$  is defined as

$$\dot{m}_s(t) = \frac{1}{L_1 L_3} \int_{L_1}^{L_1} \int_0^{L_3} c_w(x_1, x_3, t) u_s dx_3 dx_1, \quad (4)$$

where  $c_w$  is the concentration at the bottom wall. The initial value for  $m_s(t)$  is the settling velocity. It can be seen that  $\dot{m}_s(t)$  is slowly

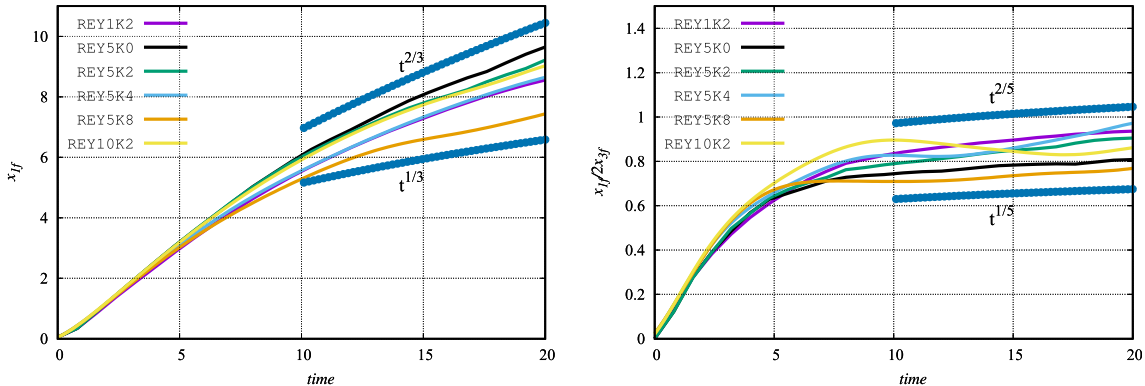


**Fig. 4.** Time evolution of the streamwise front location (left) and of the ratio between the location of the streamwise and spanwise fronts (right).

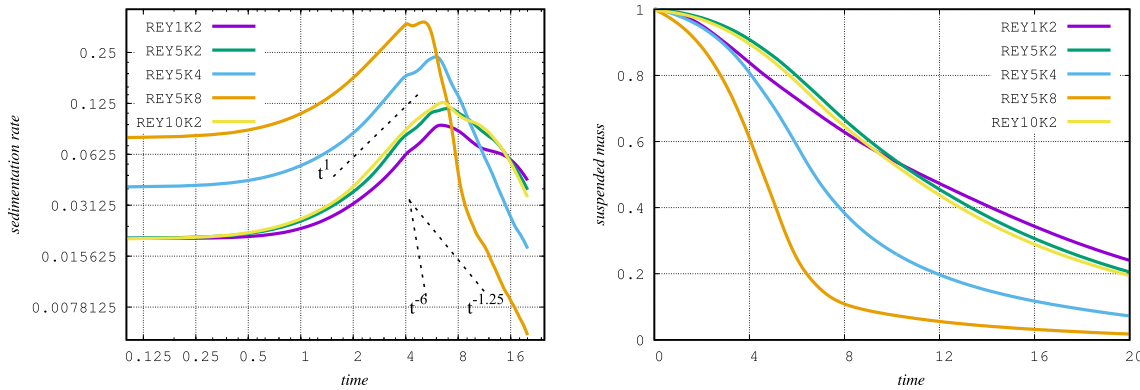


Fig. 5. Time evolution of the sedimentation rate (left) and suspended mass (right).

increasing, at a rate proportional to  $t$  (independently of the settling velocity and Reynolds number), up to  $t \approx 6.5$  where it reaches a peak value. Beyond this peak, the particles continue to deposit but at a diminishing rate, with a strong dependence to the settling velocity. As expected the peak values obtained can be directly related to the settling velocity while the dependence with the Reynolds number is insignificant. The rather fast initial rate is two times larger than the rate observed in Espath et al. (2014) for channelized gravity currents at similar Reynolds numbers. As the current starts to spread, its surface area in a basin set-up is larger than the surface area in a channel set-up (as the side walls are preventing a spanwise spreading) while the bottom concentration remains at a high level. It means that more particles will deposit in the open basin configuration. In the present work and for  $u_s = 0.02$ , the sedimentation rates are reaching values of more than 0.1 which was not the case for the channelized gravity currents in Espath et al. (2014) for the same  $u_s$ .

After the peak, the sedimentation rate is suddenly decreasing at a rate varying from  $t^{-1.25}$  (for the lowest settling velocity) to  $t^{-6}$  (for the highest settling velocity). The concentration at the bottom is more dilute with the ambient fluid and the sedimentation rate begins to decrease. Note that for a channelized current with  $u_s = 0.02$  and  $Re = 5000$  a rate of  $t^{-2.25}$  was reported in Espath et al. (2014). The simulations REY10K2 and REY5K2 are producing similar results which seems to suggest that the Reynolds number is not influencing the sedimentation rate (for the range of Reynolds numbers considered here). The key parameter with a strong influence for the sedimentation rate is the settling velocity.

The suspended mass normalized by the initial suspended mass is defined as  $m_p/m_{p_0}$  with

$$m_p(t) = \int_{\Omega} c dV. \quad (5)$$

At the end of the simulations, at  $t = 20$ , between 80% (for the lowest settling velocity) and 98% (for the highest settling velocity) of the

particles have already deposited whereas roughly 70% of the particles have deposited in the channelized simulations of Espath et al. (2014) for the same initial amount of particles. It be explained by the fact that the extend of the current at a given time is larger for the present open basin set-up than it is for the channel set-up. The decrease for  $m_p/m_{p_0}$  is quite fast before  $t \approx 8$  and then it is slowing down until the end of the simulations. Note that the influence of the Reynolds number is minimal for the temporal evolution of the suspended mass.

The potential to kinetic energy transformation is of fundamental interest in the study of gravity currents. The rate of change for the total energy is given by

$$\frac{d(k + E_p)}{dt} = - \int_{\Omega} \frac{2}{Re} \mathbf{s} : \mathbf{s} d\Omega + \int_{\Omega} \left( \frac{1}{ScRe} x_2 \nabla^2 c + x_2 u_s \frac{\partial c}{\partial x_2} \right) d\Omega = -\varepsilon - \varepsilon_s \quad (6)$$

where  $\mathbf{s}$  is the tensor of the velocity field,  $\varepsilon$  is associated to the turbulent dissipation (macro dissipation at macroscopic scale) while  $\varepsilon_s$  is the dissipation associated with loss of energy due to suspended particles (micro dissipation at microscopic scale) Espath et al. (2014).  $k(t) = \int_{\Omega} \frac{1}{2} \mathbf{u} \cdot \mathbf{u} d\Omega$  and  $E_p(t) = \int_{\Omega} cx_2 d\Omega$  are the kinetic and potential energy components, respectively. In order to study the temporal evolution of  $\varepsilon$  and  $\varepsilon_s$ , we define  $E_d$  and  $E_s$  as the time integrals of the dissipation components  $\varepsilon$  and  $\varepsilon_s$  with

$$E_d(t) = \int_0^t \varepsilon(\tau) d\tau \quad \text{and} \quad E_s(t) = \int_0^t \varepsilon_s(\tau) d\tau. \quad (7)$$

Integrating Eq. (6) in time yields the following equation

$$k + E_p + E_d + E_s = E_T = E_{T_0} = cst \quad (8)$$

where  $E_{T_0}$  is the energy available in the computational domain at the

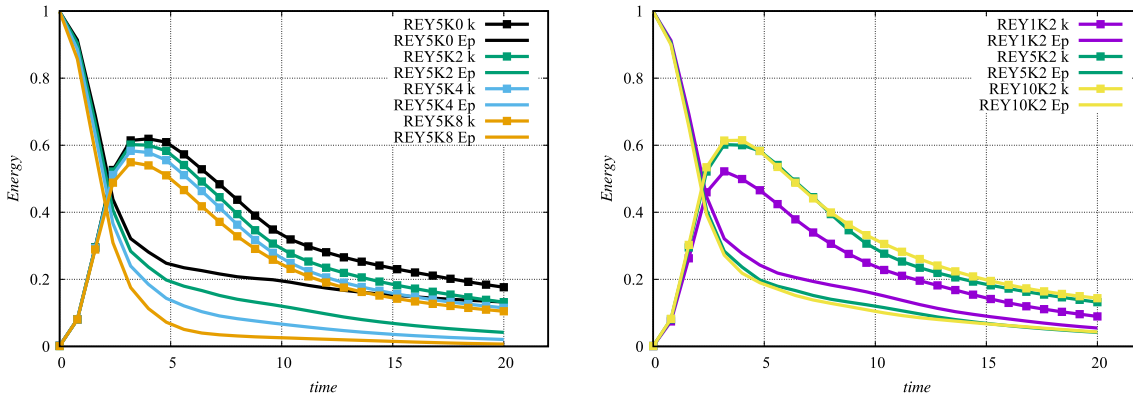
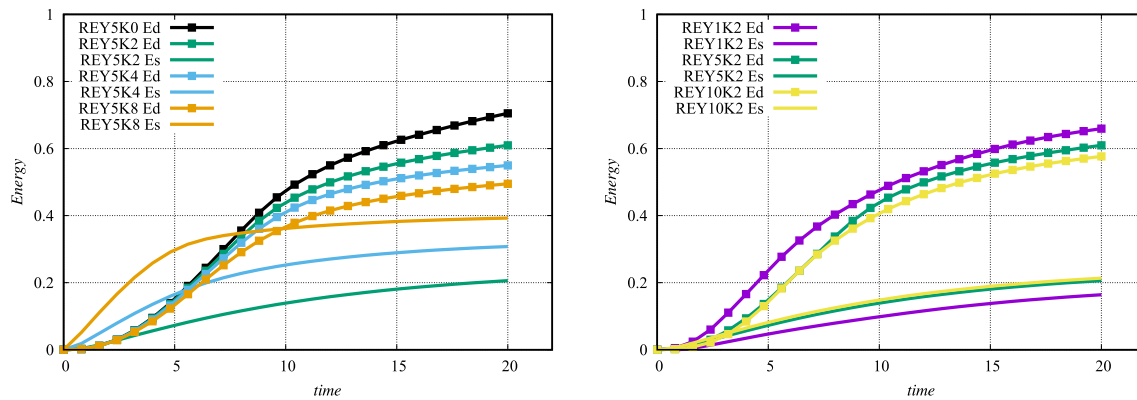


Fig. 6. Temporal evolution of the potential energy  $k$  and potential energy  $E_p$ . Left: simulations with the same Reynolds number  $Re = 5000$  (different settling velocities). Right: simulations with the same settling velocity  $u_s = 0.02$  (different Reynolds numbers).



**Fig. 7.** Temporal evolution of the turbulent dissipation  $E_d$  and particle-settling dissipation  $E_s$ . Left: simulations with the same Reynolds number  $Re = 5000$  (different settling velocities). Right: simulations with the same settling velocity  $u_s = 0.02$  (different Reynolds numbers).

beginning of the simulation.

Figs. 6 and 7 show the temporal evolution of the four terms on the left hand side of Eq. (8) normalized by  $E_{T_0}$ . Note that  $k + E_p + E_d + E_s = E_T$  is not plotted here but is within 1% of  $E_{T_0}$  at all time. A rapid conversion of potential energy into kinetic energy can be observed with a peak at  $t \approx 4$  independently of the settling velocity and Reynolds number. The decrease in potential energy, strongly linked to the settling velocity, is due to the finite nature of the lock-exchange set-up with no external source of energy available. Note that for the simulation REY5K8 the potential energy is almost zero at the end of the simulation. The peak in kinetic energy is followed by a decay in two stages: a rather fast decay from  $t \approx 4$  up to  $t \approx 10$  and then a moderate decay up to the end of the simulation. This change in decay rate, which seems independent of the Reynolds number and settling velocity, can be connected to the previously mentioned change in decay rate for the suspended mass and to the start of decay for the sedimentation rate, both occurring just before  $t \approx 8$ . After  $t \approx 10$ , not only the concentration is more diluted as 50% of the

original particles have left the computational domain. As a consequence, we can observe a decay in the driving force of the flow with less and less energy available. Surprisingly, the temporal evolution of the kinetic energy is more or less the same for  $Re = 5000$  and for  $Re = 10,000$ , even if an enhancement of turbulence was eventually expected when increasing the Reynolds number. This trend, already observed for axisymmetric currents (Zgheib et al. (2015c)) and consistent with a similar behaviour for the suspended mass, can be explained by different extents of the currents, growing at a different rate, as it will be seen later in Figure 8.

In channelized and axisymmetric currents for similar Reynolds numbers and settling velocities, the dissipation  $E_s$  related to particle-settling is dominating the dissipation  $E_d$  related to the turbulence only in the early stages of the simulation. When particles deposit at the bottom wall, the macroscopic dissipation  $E_d$  becomes the dominant dissipation term and can be two times larger than the microscopic dissipation  $E_s$  (Espath et al. (2014); Zgheib et al. (2015c)). Some of the trends observed in the present open basin set-up are radically different from the

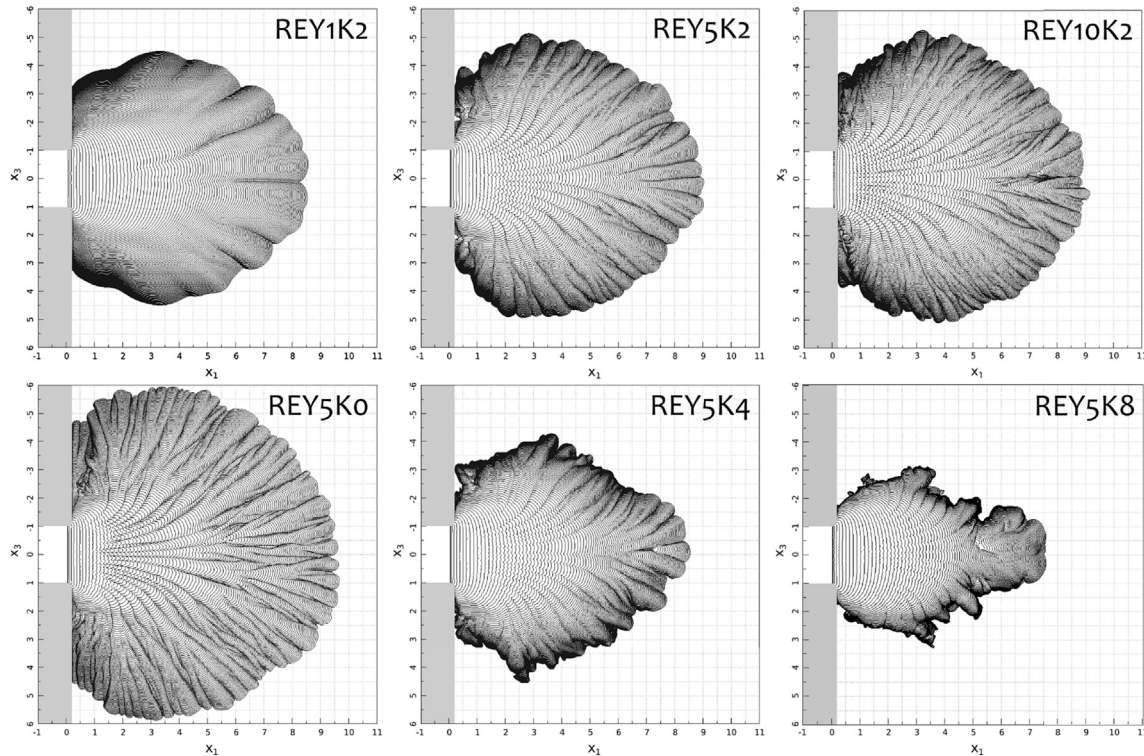


**Fig. 8.** Time evolution of isolines of the bottom wall concentration ( $c = 0.01$ ) for the six simulations (see Table 1).

**Table 2**

Summary of dimensional parameters for our study about the thickness of the deposition.

$Re$	1000	5000	5000	5000	10,000
$u_s$	0.02	0.02	0.04	0.08	0.02
$\hat{g}$ ( $m/s^2$ )	0.00052	0.0129	0.0129	0.0129	0.0518
$\hat{u}_s$ ( $m/s$ )	0.00017	0.0008	0.00161	0.00322	0.00161
$\hat{d}$ ( $\mu m$ )	16.38	35.8	50.6	71.6	50.6

behaviour of the energy budget observed in channelized gravity currents, with a strong influence of the settling velocity. For example, for all the simulations with  $u_s = 0.02$ ,  $E_d$  is always larger than  $E_s$  which is fairly low compared to channel gravity currents. Once again it is hypothesized that this is related to the surface area of the current which is much larger for the open basin than for the channel. As a consequence, the turbulent structures have more freedom to develop and can be convected in a less restrictive way than in a channel. For the simulation REY5K8, with the highest settling velocity, it can be seen that  $E_s$  becomes high very quickly and then slowly increases up to values close to 0.4 at the end of the simulation. The switch of dominance between  $E_s$  and  $E_d$  is only happening after  $t \approx 10$  which is a confirmation that the high level of particle deposition is strongly constraining the spreading of the current, confirming the trends observed in Figures 4 and 5.

## 6. Structure of the current at the wall and deposition

The formation, merging and meandering of the lobe-and-cleft structures at the front of the current can be seen in Fig. 8. When the Reynolds number is increased, the size of the lobe-and-cleft structures decreases and therefore their number increases. There is only very few large lobe-and-cleft structures at  $Re = 1000$  while the simulations at  $Re = 5000$  and  $Re = 10,000$  exhibit a large number of curved lobe-and-cleft structures of different sizes, unevenly distributed radially. The observed slightly curved structures are different from the straight ones obtained with an axisymmetric lock (Cantero et al. (2007a)), which are aligned with the

current local direction of expansion. Such curved lobe-and-cleft structures were reported very recently in Zgheib et al. (2015a) for non-circular releases of rounded-rectangular shape. They can be attributed to different radial spreading rates. When the settling velocity is increased the lobe-and-cleft structures are dramatically impacted with fewer and smaller structures as a result of a substantial reduction in the current spreading. The sedimentation seems to prevent some interactions among the lobe-and-cleft structures.

In order to better understand the influence of the Reynolds number and settling velocity on the temporal evolution of the currents, it could be interesting to compare their areas as a percentage of the computational domain. This can be easily achieved by using the last isoline obtained at  $t = 20$ . For the conservative simulation REY5K0 the current covers 70.3% of the computational domain whereas for the simulation REY5K8 (same Reynolds number but higher  $u_s$ ) the current covers only 24.2% of the computational domain. An interesting feature is that the settling velocity is mainly slowing down the current in the spanwise direction. As far as the Reynolds number is concerned (and for the same settling velocity), the extend of the current is almost the same between the simulation REY5K2 and the simulation REY10K2 with the current covering 53% and 55% of the computational domain, respectively.

Dimensional quantities (denoted with a hat) can be used to investigate about the thickness of the deposition. To relate our simulations to a typical laboratory-scale experiment, we choose a vertical dimension  $L_2$  of  $2\hat{h} = 0.25m$ . We assume that the ambient fluid is water ( $\hat{\rho}_{fluid} = 1000kg/m^3$ ,  $\hat{v} = 10^{-6}m^2/s$ ) and the density of the particle is  $\hat{\rho}_{part} = 2650kg/m^3$  (a value representative of gravity currents, see Normark et al. (1993)). The reduced gravity  $\hat{g}$ , settling velocities and diameters of particles can be found in Table 2.

2D maps of the wall deposition, defined as

$$D_i(x_1, x_3, t) = \frac{c_i}{\sigma} \int_0^t c_w(x_1, x_3, \tau) u_s \, d\tau \quad (9)$$

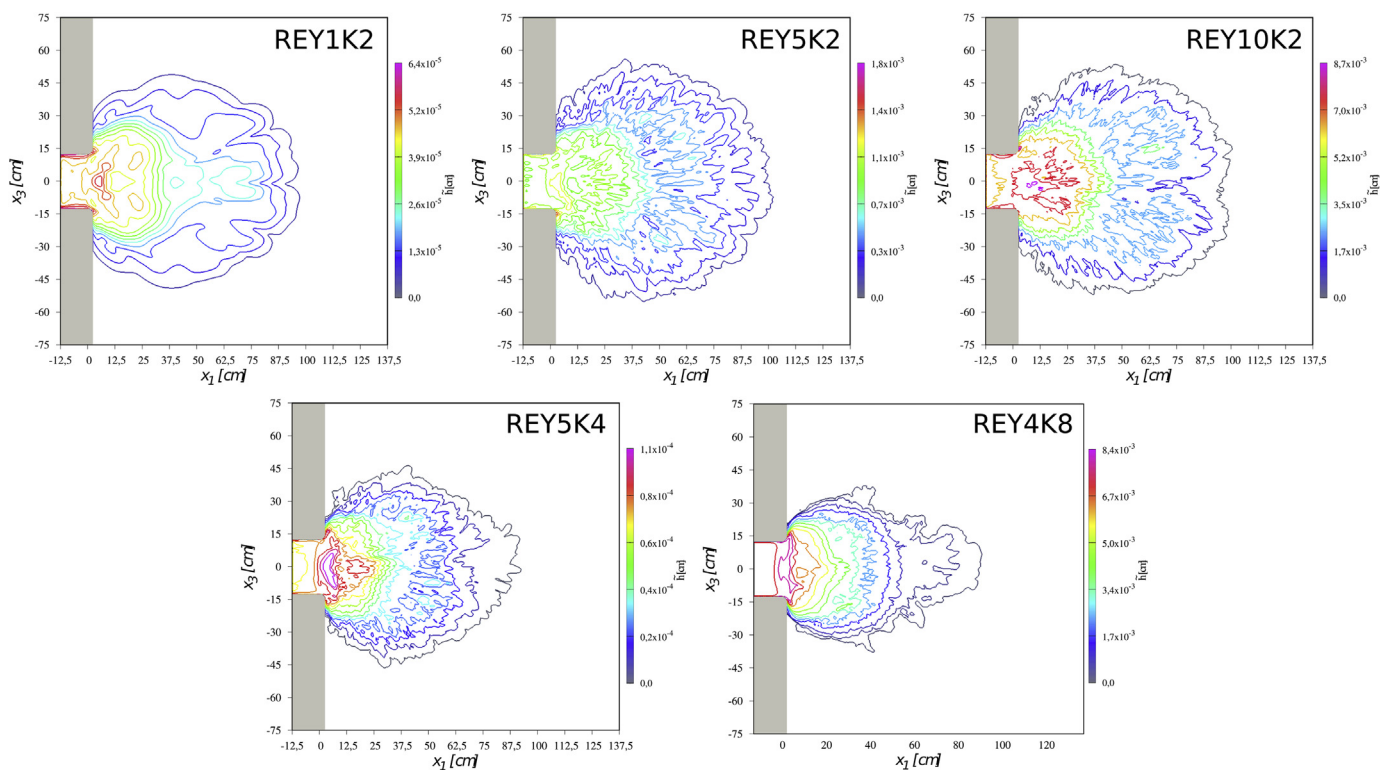


Fig. 9. 2D deposit maps from  $t = 5$  to  $t = 20$  for the five non-conservative simulations (red is the maximum value, blue is 0). (For interpretation of the references to colour in this figure legend, the reader is referred to the web version of this article).

where  $\sigma$  is defined as the packing fraction of the settled sediment, are presented in Fig. 9 at  $t = 20$ .  $\sigma$  typically takes an approximate value of 0.63 (Nasr-Azadani et al. (2013)). However, as we are not concerned with the porosity of the sediment layers in the present study, we simply set  $\sigma = 1$ . For the lowest Reynolds number (simulation REY1K2), the deposition pattern is still symmetric with large lobe-and-cleft structures. For the simulation REY10K2, a large-scale bifurcation seems to split the deposit map in two large areas (for  $x_3 = 0$  cm and  $x_1 \approx 87$  cm). Such bifurcations are often observed in nature as seen in Fig. 3 of Twichell et al. (1992). We are currently running a stability analysis to fully understand the origin of this bifurcation which seems to happen only at large Reynolds numbers. Such stability analysis is beyond the scope of the current study.

One important result is the high levels of deposition very close to the initial reservoir, especially when the settling velocity is large. The maximum deposition height for the simulation REY5K8 is more than five times higher than the maximum deposition height reported in the simulation REY5K2. The deposition maps obtained for simulations REY5K2 and REY10K2 are showing that when the Reynolds number is increased the deposition process is less intense near the gate and the particles are more likely to travel downstream of the initial reservoir. This can be related to a more turbulent flow when the Reynolds number is increased, with particles more likely to be convected downstream in vortical structures. These results are drastically different from the ones obtained for a channel where a streamwise wavy behaviour was observed in Espath et al. (2014, 2015) for the deposition maps at the bottom wall, with intense levels of deposition at a streamwise distance of about 3h and 6h from the gate.

## 7. Conclusion

We have presented original high-fidelity simulations for an open basin lock-exchange configuration for which the geometry is representative of the geometry of some real-life turbidity currents such as deltas at the mouth of rivers. Our basin currents exhibit many differences with channelized or axisymmetric lock-exchange configurations reported previously in the literature. They consist of an alternation of intense and quiet areas. The quiet areas are characterized by the absence of vortical structures while the intense areas are characterized by a large density of multi-scale vortical structures. Those structures in the intense areas are directly related to high levels of particles concentration. The sedimentation rates observed in this study are much faster than the ones obtained in channelized configurations, with a strong influence of the settling velocity. When the settling velocity is increased, important reduction of the front extent is observed in the spanwise direction whereas the streamwise extent of the current remains more or less unaffected. The influence of the Reynolds number on the sedimentation rate and suspended mass is very limited. One important result is that, unlike channelized gravity currents, the macroscopic dissipation  $E_d$  is not necessarily the dominant dissipation term when particles deposit at the bottom wall. When the Reynolds number is increased, the currents exhibit a large number of curved lobe-and-cleft structures of different sizes, unevenly distributed radially, different from the straight ones observed in axisymmetric currents. The sedimentation seems to control the development of the lobe-and-cleft structures with a strong reduction of their size, especially in the spanwise direction. Finally, we observe a large-scale bifurcation on the deposit map for the simulation with the highest Reynolds number, very similar to what is observed in nature. Its origin is yet to be discovered.

Assuming that our basin currents will eventually become axisymmetric currents (which is not guaranteed and which is not yet the case according to Fig. 4), future polydisperse (various particles sizes at the same time) studies with a larger and longer computational domain (requiring very expensive high-fidelity simulations) will be carried out to determine at which radial distance our currents are eventually transitioning to axisymmetric currents. Finally, we are currently developing a

new framework based on a customized Immersed Boundary Method where the height of deposition at the bottom floor can be taken into account in order to add more realistic features to our approach.

## Acknowledgements

The authors are grateful to Dr. Carlos Moser for many interesting discussions. Present simulations have been carried out at the Pontifícia Universidade Católica do Rio Grande do Sul (PUCRS) High Performance Computing facility LAD and on ARCHER in the UK. Sylvain Laizet also acknowledge the EPSRC UK Turbulence Consortium (Research grant EP/L000261/1) for access to UK supercomputing resources. The authors are grateful to Petrobras (0050.0092355.14.9) for supporting this research.

## References

- Barley, B., 1999. Deepwater problems around the world. *Lead. Edge* 18 (4), 488–493.
- Bonacaze, R., Hallworth, M., Huppert, H., Lister, J., 1995. Axisymmetric particle-driven gravity currents. *J. Fluid Mech.* 294, 93–121.
- Cantero, M., Balachandar, S., García, M., 2007a. High-resolution simulations of cylindrical density currents. *J. Fluid Mech.* 590, 437–469.
- Cantero, M., Balachandar, S., García, M., Bock, D., 2008. Turbulent structures in planar gravity currents and their influence on the flow dynamics. *J. Geophys. Res.* 113 (C8).
- Cantero, M., Balachandar, S., García, M., Ferry, J., 2006. Direct numerical simulations of planar and cylindrical density currents. *J. Appl. Mech.* 73 (6), 923–930.
- Cantero, M., Lee, J., Balachandar, S., García, M., 2007b. On the front velocity of gravity currents. *J. Fluid Mech.* 586, 1–39.
- de Rooij, F., Dalziel, S., 2001. Time- and space-resolved measurements of deposition under turbidity currents. *Spec. Publ. Int. Ass. Sediment.* 31, 207–215.
- Espath, L., Pinto, L., Laizet, S., Silvestrini, J., 2014. Two- and three-dimensional direct numerical simulation of particle-laden gravity currents. *Comput. Geosci.* 63, 9–16.
- Espath, L., Pinto, L., Laizet, S., Silvestrini, J., 2015. High-fidelity simulations of the lobe-and-cleft structures and the deposition map in particle-driven gravity currents. *Phys. Fluids* 27 (5), 056604.
- Härtel, C., Carlsson, F., Thunblom, M., 2000a. Analysis and direct numerical simulation of the flow at a gravity-current head. Part 2. The lobe-and-cleft instability. *J. Fluid Mech.* 418, 213–229.
- Härtel, C., Meiburg, E., Necker, F., 2000b. Analysis and direct numerical simulation of the flow at a gravity-current head. Part 1. Flow topology and front speed for slip and no-slip boundaries. *J. Fluid Mech.* 418, 189–212.
- Hoult, D., 1972. Oil spreading on the sea. *Ann. Rev. Fluid Mech.* 4 (1), 341–368.
- Huppert, H., Simpson, J., 1980. The slumping of gravity currents. *J. Fluid Mech.* 99 (04), 785–799.
- Julien, P., 2010. Erosion and Sedimentation. Cambridge University Press.
- Kuenen, P., 1951. Properties of turbidity currents of high density. *Spec. Publ. SEPM* 2, 14–33.
- Laizet, S., Lamballais, E., 2009. High-order compact schemes for incompressible flows: a simple and efficient method with the quasi-spectral accuracy. *J. Comp. Phys.* 228, 5989–6015.
- Laizet, S., Li, N., 2011. Incompact3d: a powerful tool to tackle turbulence problems with up to  $O(10^5)$  computational cores. *Int. J. Heat Fluid Flow* 67, 1735–1757.
- Luthi, S., 1981. Experiments on non-channelized turbidity currents and their deposits. *Mar. Geol.* 40(3) (3), M59–M68.
- Meiburg, E., Kneller, B., 2009. Turbidity currents and their deposits. *Ann. Rev. Fluid Mech.* 42, 135–156.
- Middleton, G.V., 1993. Sediment deposition from turbidity currents. *Annu. Rev. Earth Planet. Sci.* 21, 89–114.
- Nasr-Azadani, M., Hall, B., Meiburg, E., 2013. Polydisperse turbidity currents propagating over complex topography: comparison of experimental and depth-resolved simulation results. *Comput. Geosci.* 53, 141–153.
- Necker, F., Hartel, C., Kleiser, L., Meiburg, E., 2002. High-resolution simulations of particle-driven gravity currents. *Int. J. Multiph. Flow* 28, 279–300.
- Normark, W., Posamentier, H., Mutti, E., 1993. Turbidite systems: state of the art and future directions. *Rev. Geophys.* 31 (2), 91–116.
- Parnaudeau, P., Carlier, J., Heitz, D., Lamballais, E., 2008. Experimental and numerical studies of the flow over a circular cylinder at Reynolds number 3 900. *Phys. Fluids* 20, 085101.
- Parsons, J., Friedrichs, C., Traykovski, P., Mohrig, D., Imran, J., Syvitski, J., Parker, G., Puig, P., Buttles, J., Garcia, M., 2007. The Mechanics of Marine Sediment Gravity Flows. *Continental Margin Sedimentation*, 37. IAP Special Publication, pp. 275–338.
- Rocca, M.L., Adduce, C., Sciotino, G., Pinzon, A., 2008. Experimental and numerical simulation of three-dimensional gravity currents on smooth and rough bottom. *Phys. Fluids* 20 (10), 106603.
- Rocca, M.L., Adduce, C., Sciotino, G., Pinzon, A., Boniforti, M., 2012. A two-layer, shallow-water model for 3d gravity currents. *J. Hydraulic Res.* 50 (2), 208–217.
- Rottman, J., Simpson, J., 1983. Gravity currents produced by instantaneous releases of a heavy fluid in a rectangular channel. *J. Fluid Mech.* 135, 95–110.
- Talling, P.J., Masson, D.G., Sumner, E.J., Malgesini, G., 2012. Subaqueous sediment density flows: depositional processes and deposit types. *Sedimentology* 59 (7), 1937–2003.

- Twichell, D., Schwab, W., Nelson, C., Kenyon, N., Lee, H., 1992. Characteristics of a sandy depositional lobe on the outer Mississippi fan from seamarc ia sidescan sonar images. *Geology* 20 (8), 689–692.
- Ungarish, M., 2009. An Introduction to Gravity Currents and Intrusions. CRC Press.
- Zgheib, N., Bonometti, T., Balachandar, S., 2014. Long-lasting effect of initial configuration in gravitational spreading of material fronts. *Theor. Comp. Fluid Dyn.* 28 (5), 521–529.
- Zgheib, N., Bonometti, T., Balachandar, S., 2015a. Dynamics of non-circular finite-release gravity currents. *J. Fluid Mech.* 783, 344–378.
- Zgheib, N., Bonometti, T., Balachandar, S., 2015b. Propagation and deposition of non-circular finite release particle-laden currents. *Phys. Fluids* 27 (8), 086604.
- Zgheib, N., Bonometti, T., Balanchandar, S., 2015c. Direct numerical simulation of cylindrical particle-laden gravity currents. *Comput. Fluids* 123, 23–31.